Final Report to

Asian Office of Aerospace Research & Development

Generation of Controllable Time-Mean Microvortices to Mimic Insect Flights

by

Andrew M. Wo, Ph.D.

Professor

Institute of Applied Mechanics,

National Taiwan University, Taipei, Taiwan

Andrew@iam.ntu.edu.tw

January 2010

Report Documentation Page		*Form Approved* *OMB No. 0704-0188*

Public reporting burden for the collection of information is estimated to average 1 hour per response, including the time for reviewing instructions, searching existing data sources, gathering and maintaining the data needed, and completing and reviewing the collection of information. Send comments regarding this burden estimate or any other aspect of this collection of information, including suggestions for reducing this burden, to Washington Headquarters Services, Directorate for Information Operations and Reports, 1215 Jefferson Davis Highway, Suite 1204, Arlington VA 22202-4302. Respondents should be aware that notwithstanding any other provision of law, no person shall be subject to a penalty for failing to comply with a collection of information if it does not display a currently valid OMB control number.

1. REPORT DATE **04 FEB 2010**	2. REPORT TYPE **FInal**	3. DATES COVERED **01-06-2008 to 01-01-2010**
4. TITLE AND SUBTITLE **Generation of Controllable Time-Mean Microvortices to Mimmic Inset Flights**		5a. CONTRACT NUMBER **FA23860814067**
		5b. GRANT NUMBER
		5c. PROGRAM ELEMENT NUMBER
6. AUTHOR(S) **Andrew Wo**		5d. PROJECT NUMBER
		5e. TASK NUMBER
		5f. WORK UNIT NUMBER
7. PERFORMING ORGANIZATION NAME(S) AND ADDRESS(ES) **National Taiwan University, 1 Roosevelt Road, Section 4,Taipei 106,Taiwan,TW,106**		8. PERFORMING ORGANIZATION REPORT NUMBER **N/A**
9. SPONSORING/MONITORING AGENCY NAME(S) AND ADDRESS(ES) **AOARD, UNIT 45002, APO, AP, 96337-5002**		10. SPONSOR/MONITOR'S ACRONYM(S) **AOARD**
		11. SPONSOR/MONITOR'S REPORT NUMBER(S) **AOARD-084067**

12. DISTRIBUTION/AVAILABILITY STATEMENT **Approved for public release; distribution unlimited**
13. SUPPLEMENTARY NOTES
14. ABSTRACT **This report presents a study of a novel mechanism (microvortices) to generate lift towards application in micro air vehicle (MAV). The mechanism of vortex generation considered is in-plane oscillation of a flat plate with suitable structure on the plate?s top surface. Methodologically, experimental approach is first commenced followed by compution to study a wide range of parameter space. The microdevice leverages on Lorentz force to drive the suspended MEMs-based microplate to in-plane resonance.**
15. SUBJECT TERMS **Fluid Mechanics, Micro Air Vehicles (MAVs), Microvortices, acoustic streaming, micro fluidics**

16. SECURITY CLASSIFICATION OF:			17. LIMITATION OF ABSTRACT	18. NUMBER OF PAGES	19a. NAME OF RESPONSIBLE PERSON
a. REPORT **unclassified**	b. ABSTRACT **unclassified**	c. THIS PAGE **unclassified**	**Same as Report (SAR)**	**36**	

Standard Form 298 (Rev. 8-98)
Prescribed by ANSI Std Z39-18

Executive Summary

This report presents a study of a novel mechanism to generate lift towards application in micro air vehicles (MAV). To achieve this aim, the overarching emphasis is to characterize microvortices and associated lift forces under a range of conditions. The mechanism of vortex generation considered is in-plane oscillation of a flat plate with suitable structure on the plate's top surface. This mode of oscillation should be simple to implement in actual practice, and does not require asymmetric flapping of flexible wing. Methodologically, experimental approach is first commenced followed by computation to study a wide range of parameter space. The microdevice leverages on Lorentz force to drive the suspended MEMS-based microplate to in-plane resonance. Briefly, AC current flows through suspended beam-like microelectrode structure – a microplate is supported by one cantilever beam on each side – with an external magnetic field underneath. The net result is in-plane, lateral motion of the microplate. As a result, the observed flow features are time-mean microvortices. Computational effort centers around optimization of a range of parameters (geometry, frequency, amplitude of oscillation, etc.) to generate time mean lift. Suitable structures are placed on the upper side of the otherwise flat plate to facilitate time-mean vortex formation.

Results suggest the mechanism of time-mean vortex generation under periodic in-plane oscillation of a flat plate is predominantly due to nonlinear effect of acoustic streaming near the finite edges. With this understood, the approach is then to generate multiple vortices through spatial geometric variation on the plate. Extrusion extended vertically from the plate is adopted for simplicity and, hence, ease of practical implementation. Relationship between vortices, pressure distribution and resultant lift are characterized through a range of parameter space. Net lift is found for cases where frequency is high and under large oscillation amplitude. The results should be applicable to realization of lift on MAV since a relatively simple mechanism of in-plane oscillation of a tuned structure is considered quite feasible.

1. Introduction

Vortices are as old as fluid mechanics. Much work has been done on almost all aspect of the flow phenomenon for the past fifty years. For instance, topics reviewed by *Annual Review of Fluid Mechanics* include transition beneath vortical disturbances [1], airplane trailing vortices [2], vorticity dynamics of the oceanic general-circulation [3], and many more.

However, generation of microvortices (order of tens of microns or smaller) is difficult at best, with dominant contribution from the microfluidics community (see [4-5] for review on microfluidics). There are essentially two categories of generation of microvortices: electrokinetic-based approach and confined-cavity approach. Electrokinetic-based approach utilizes interaction of electrolyte medium with the imposed AC or DC electric field [6-9]. Microvortices are formed when the medium takes on a particular trajectory dictated by the unique shape of the electrode, e.g. ring shape. Although these designs serve the various applications of concern, the nature of the generation of microvortices is strongly dependent upon the solution medium and electrode design, thus limiting its utilization. On the other hand, the confined-cavity approach [10-12] in generating microvortices uses shear stress through an opening in a microchannel to drive the flow within a confined square, or circular, cavity. Although this approach is independent of medium/electrode combination, the microvortices are encapsulated with wall boundaries.

Efficient generation of lift on a MAV is a major technological challenge [13-15]. Flapping wing is more efficient in specific power requirement at low speed than either fixed- or rotary-wing flight. The key feature of lift generation in MAV is the vortex system involving both the bound vortex and shed vortices in an unsteady manner. To illustrate this point, the ratio of instantaneous to steady circulation for a 2D bound/shed vortex system ranges from 0 to close to 1 in approximately five chord lengths [16]. This is indicative that circulation changes in a sufficient rapid manner that the bound/shed vortex system – not an individual vortex – must be considered in

an unsteady manner. This is the case not just in a 2D vortex system but in a much more complicated 3D system as well [17]. Consideration of the lift-drag polar provides additional evidence that this vortex system is of prime importance [16]. The scenario that provides the maximum lift-drag ratio is due to that of flapping wing configuration, where non-flapping wing cases result in substantially less performance. Thus overwhelming evidences suggest that vortex-generated lift is of considerable advantage for lift generation for MAV applications. However, flapping wing involved much inherent mechanical complexity. Thus an alternative approach for lift generation in MAV is under studied.

This report presents a method of generating time-mean vortices via a microplate under in-plane oscillation, see Fig. 1. The motivation stems from utilization of the phenomenon of acoustic streaming [17-18], or flow streaming as referred to in some literature, to achieve time-mean vortical features from AC actuation. Acoustic streaming arises when the non-linear convective terms in the Navier-Stokes equation contain non-zero time-mean contributions. These contributions are then balanced by the time-mean pressure, and results in DC streaming flow. This method entirely circumvented the limitations of the two aforementioned approaches and allows generation of microvortices for almost all fluid medium in an open region. Both experimental and numerical approaches are utilized to tackle the physics involved.

2. Experimental Aspects

2.1   Design of the microdevice

Lorentz force is utilized to drive a microplate to resonance at approximately 140 kHz with one distinct advantage of reducing the complexity of device actuation, instead of embedding the excitation source within the chip, see Fig. 1. Once in resonance, the microplate generates two microvortices near its edges via secondary flow phenomenon of acoustic streaming.

The main structure of the vortices generator consists of a double-clammed, suspended bridge,

combined with a square plate in the middle, as the primary structure, as shown in the 3D sketch of Fig. 1a. When an alternating current (AC) passed through the gold layer on the surface of the suspended bridge in the presence of an external magnetic field B (Nd-Fe-B magnet, < 1 Tesla) perpendicular to the bridge surface, the main structure was forced to oscillate in the third (in-plane) direction. The geometry of the bridge is 1.2μm thick, 20 μm wide, and 750 μm long, with the square microplate (100 μm by 100 μm) in the middle. Figure 1b shows an edge-on view of the micro structure.

This design is distinct from that of Lutz. et al. [20] in several ways. First, the method of generation is entirely different: the driving source is embedded within the present device verses external. Second, the region where cells are trapped is in the outer streaming flow in this study verses within the inner eddies. Third, the frequency of oscillation being fixed 140kHz vs. 40Hz. to 1kHz. These differences have consequences in the entire flow field, and, more importantly, on the trapped bioparticles, e.g. shear stress, as will be discussed below.

2.2   Quality factor of the microdevice

This vortices-generator is a resonant-based actuator operating under liquid with the natural frequency around 140 kHz. This is implied from the rotational velocity of the vortices which maximizes at this frequency, and decays substantially at off-peak frequencies. The maximum displacement of the oscillatory plate is less than 1μm. From this spectral information, the quality factor (Q) is calculated to be about 10, which is indicative of a reasonable resonating device. For further details in the design of the microdevice, please refer to [21-22].

2.3   Device fabrication

The suspended structure was fabricated in three steps: thin film deposition, lithography and etching. Each of which will be described in some detail below.

2.3.1 Thin film deposition

With silicon as substrate, the suspended microplate was fabricated from silicon nitride (~1μm), deposited by low pressure chemical vapor deposition system (LPCVD) around 800°C. After completing the thin film deposition, the wafer was placed in E-beam evaporator at low pressure for sputtering the metallic layer onto the wafer surface as electrode. The order of metal to deposit is first chromium (~100 Å thick) then gold (~1500 Å thick) to leverage the chromium layer as adhesion between silicon nitride and gold.

2.3.2 Lithography

In order to define the suspended structure, two masks are needed in the photolithographic process. Thin positive photoresist (Shipley 1813) is used to coat ~1.3μm thickness on the metallic layer by using a spin coater. The spin procedure of the PR layer is to increase to 800RPM at acceleration of 200 RPM/s and hold for 10 seconds. The second step is to further increase to 4000RPM at acceleration 400 RPM/s and hold for 30 seconds. Then, the wafer was heated by a hot plate at 90°C for 100 seconds. Afterwards, the device was exposed through the first mask by utilizing the UV light (wavelength 365nm) which power is around 15mJ/cm^2 for 5.5 seconds to define the primary microelectrode structure. Developer (MF-319) removed the exposure area when the device was immersed for 1 minute, then stop-develop using DI water to rinse the surface and N$_2$ gas dry. The chip was baked at 100°C for 5 minutes to reduce residual solvent.

The purpose of the second mask is to define the cavity underneath the structure, and the total length (750μm) of the beam and the overall features. By repeating the procedure of coating photoresist (S1813), the second mask targets on the key that represents the second pattern has matched with the first pattern. Also, the UV light (wavelength 365nm, power 15mJ/cm^2) was used through the mask for 5.5 seconds, and the chip was subsequently developed by developer (MF-319). Finally, the structure was checked by microscope to make sure the photoresist cover the entire electrode.

2.3.3 Etching

The purpose of the etching steps is to suspend the microplate structure. Silicon nitride that is not protected by the photoresist need to be etched using reactive ion etching (RIE). During which, CF_4 gas is chosen and includes four parameters: (1) pressure of 7.8 Pa, (2) flow rate of 50 sccm, (3) power of 70 W, and (4) time of 18 minutes.

Next, the unprotected region in the silicon nitride would be etched by potassium hydroxide (KOH). The chip is immersed into alkaline solution whose prescription is KOH：DI water = 1：4. Moreover, the probe temperature is set at 78°C and stirring rod rotating at 180rad/s for 12hours. Finally, the chip is rinsed by DI water and dried by N_2 gas. Fabrication of the suspended structure is then completed.

3. Computation effort

The computation allows numerical experiment to explore a range of parameter space – including various geometric details, frequency, amplitude of oscillation – in order to optimize lift. The workhorse computational tool, Comsol Multiphysics (Comsol Inc.), allows almost seamless integration of a range of physics for microfluidic calculations (although not fully utilized for this work). Ability to generate unstructured grid with relative ease is a substantial benefit, allowing exploration of various geometry to maximize vortex formation, hence lift, without concern of subsequent grid generation. The code also features ability to perform post-processing of data, which substantial aids interrogation of results for design purpose.

4. Experimental Results

The dominant effect of the oscillatory microplate's boundary, other than the classical Stokes-like unsteady boundary layer with penetration depth of ~6μm, is generation of a pair of 2D, large-scale, time-mean, counter-rotating microvortices. Figure 3 presents micrograph of the microvortices with diameter of 80-100μm (order of the microplate dimension), as made evident

through polystyrene tracer particles (10μm) in circular trajectory. Majority of the particles are initially drawn from far above the plate toward the plate center, then, as they approach the surface, directed toward the two edges, ejected outward, looped upward, and re-circulated back towards the plate center – repeating the trajectory. Small number of particles, however, are ejected far beyond the plates' edges and never to return. This data show the microvortices are robust and controllable.

Preliminary computation effort supports the experimental findings and provide further insight. Figure 4 presents the computed *time-mean* streamline in the region above the oscillatory microplate. Distinct, symmetric, circulatory streamline patterns are shown. Streamlines are far above the plate and directing toward the center, entering the tight vortex core, with some leaving the core at the far ends while majority of the flow forms the re-circulating pattern. Streamline pattern further suggests large variation of velocity over the plate; streamlines conglomerate just above the plate indicating high-speed flow and are further apart at the top of the vortex. Overlay the trajectory of tracer particles from Fig. 3 onto the computed streamlines shows the two flow patterns agree well. The computation is thus believed to be capable of capturing the dominant physics, although further study is needed.

Rotational velocity of the microvortices should play a key role in defining the characteristics of the microvortices. Figure 5 presents the results of rotational velocity for a range of driving voltage of the microplate. The average rotational velocity is in the order of hundreds to a thousand microns per second, which is a relatively fast value in microflow environment, and varies quadratically with driving voltage, having a threshold voltage of 2 Vpp. The second ordinate shows the rotational *frequency* of the microvortices, with maximum frequency of about 6 Hz at 9 Vpp. Results showed the relationship between rotational velocity and driving voltage to be essentially equivalent to that of using polystyrene beads. In this work, with the geometry of the microplate and the frequency fixed, the variation of rotational velocity with voltage is largely due to variation of oscillatory amplitude with voltage (also see Schlichting [19]).

It is interesting to note that the *theoretical* magnitude of the rotational (streaming) velocity does not depend on viscosity. Schlichting's analysis of successive approximation (his eqn. (15.63) [19]) shows the streaming flow u_2 far from the surface is:

$$u_2(x,\infty) = -\frac{3}{4}\frac{U_0}{n}\frac{dU_0}{dx},\qquad(1)$$

where Uo is the velocity amplitude outside of the viscous region, n the radian frequency, and x the direction along the moving surface. Note that the eqn. above does not contain the viscosity directly. Viscosity affects the rotational velocity since it is a parameter in the time-averaged governing equation for the streaming flow. Physically, as the driving voltage increases, both the Lorentz force and the fluid temperature increase. This results in two effects: (1) the increase in Lorentz force causes an increase in the plate's amplitude, and (2) the increase in temperature lowers the viscosity, which would further increase the amplitude due to decrease in viscous damping. Hence, both effects would contribute to the rotational velocity vs. voltage data. However, we believed that the first effect dominates, as suggested by the non-linear role of amplitude.

5. Computational Results

With the definitive pair of vortices captured by the experiment, computational effort was commenced to explore vortical flow features that would maximize lift. To this end, a range of parameter space was studied. This includes asymmetric geometry between the upper and lower surfaces, frequency and amplitude of oscillation. Decision to embrace this set of variables was guided by physical intuition and non-dimensional analysis.

The moving-mesh technique was utilized for describing the oscillatory boundary in an unbounded half-space field with air as working fluid (ρ =1.0 Kg/m3, ν =1.8e-5 Pa • s). The range of oscillating frequency of the moving plate studied was 1Hz, 10Hz, 100Hz, and 1000Hz. The thickness of the plate (t) is kept fixed at 1 mm. The amplitude of oscillation ranges from 0.1 m (0.1t), 0.2 mm (0.2t), and 0.5 mm (0.5t). Time-mean velocity field, time-mean pressure, and

time-mean total force per unit depth were reported at time interval of T*/N (T*= 1/frequency, N= 50, where the N is the number of time steps per cycle) by solving the incompressible Navier-Stokes equation for 20 cycles of oscillation.

As aforementioned, systemic computational study of a range of parameter space was untaken. First, flat plate under in-plane oscillation was commenced which serves as control for subsequent calculations. Figure 6a presents the mesh and the range of physical parameters studied. The geometric parameters include plate thickness (t)= 1mm (fixed); length of plate= 30mm; frequency= 100Hz; amplitude ratio (δ/t)= 0.1, 0.2, 0.5. Much effort was spent to fine-tune the computation to allow for convergence in this 2D unsteady calculation while maximizing grid density.

Figure 6b shows the computed flow features near the right edge of the flat plate. As aforementioned, edge effect plays a key role in lift generation and, as expected, poses difficulty due to singularity involved, requiring special care in handling the numeric. Much effort in trial and error was exerted. Velocity vector results show clear vortical flow features. Due to symmetry of the top and bottom geometry, distinct, symmetric, circulatory flow patterns are also demonstrated. The flow above the plate is directed toward the pate's edge, entering the tight vortex core and forming the re-circulating pattern. The velocity vector pattern further suggests large variation of velocity over the plate; corresponding streamlines conglomerate just above the plate indicating high-speed flow and are further apart at the top of the vortex. The computation is thus believed to capture the dominant physics.

Figure 6c shows the time-mean pressure on the plate's top and bottom surfaces. Results indicate distinct low pressure regions near plate's edges, corresponding to the presence of the vortices on the two surfaces. This further confirms the argument that non-linear acoustic streamlining in the vicinity of the finite edges is the main culprit for the generation of time-mean vortices under purely periodic motion. Although, as expected, the pressure on the top and bottom surfaces are identical hence no net pressure difference across the flat plate, this result suggests that

"finiteness of geometry" can be beneficial towards lift generation. Subsequent choice of potential geometry that might incur lift is motivated by this observation.

Figure 6d presents the time excursion of the integrated unsteady force (per unit depth) on the flat plate. Data suggest that the force variation follows a periodic nature with negligible time-mean, if any at all. The numerics of time-mean lift indeed prove to be negligible – on the order of numerical error – even at 100Hz and amplitude ratio of 0.0002 and 0.0005. This is understandable based on physical ground: top and bottom surface of the plate is symmetrical.

With the understanding of the flat plate baseline case, insight on the importance of the finiteness of the edges is gained. Leveraging upon this, subsequent design is focused on encouraging geometric spatial gradient along the plate in order to produce vortices, hence should develop lift. To first test this approach, the two edges is designed with vertical extrusion (tip structure) from the edge pointing upward. This design will break the symmetry between the top and bottom surfaces. Further details are provided below.

Figure 7 presents calculations with two extrusion structure placed on each of the two edges to encourage spatial gradient, while the entire structure undergoes in-plane periodic oscillation (see Fig. 7a). Figures 7b and 7c present the captured vortices near the tip edges. Distinct vortical flow features can be seen, each on each side of the extrusion. Resulting pressure distribution further confirms the two vortices via spikes in the signature, as shown in Fig. 7d. Figures 7e to 7g reveal force excursion over the period of unsteadiness corresponding to 100Hz. and increasing amplitude of oscillation from 0.1t, 0.2t, to 0.5t. The trend of increasing lift as amplitude increases is clearly established.

Figure 8 corresponds to having the extruding structure *on* the plate – not just at the edges (see Fig. 8a). This set of results – see Fig. 8b for vortex structure, Fig. 8c for pressure signature, and Fig. 8d for force excursion – all suggest similar trend as that for the extrusion near the edges. This set of results further encourages the use of extruding structure over the entire plate to further maximize lift over the entire plate surface.

Figure 9 presents 2D flat plate under in-plane periodic oscillation with multiple extruding structures on the plate (see Fig. 9a). Parameter space studied include: plate thickness (t)= 1mm (fixed); length of plate= 34mm; distance between extruded structure (h)= 2t; frequency= 1, 10, 100, 1000Hz; amplitude ratio (δ/t)= 0.1, 0.2, 0.5. Figure 9b shows repeated pressure signature – now seems obvious – corresponding to the vortices induced by the extrusion. Integrated force over a range of amplitudes are presented in Figs. 9c to 9k. Table 1 summarized the calculated force for the nine cases. Results confirmed that lift increases as both the frequency and oscillation amplitude increase. The maximize lift computed reaches ~$3.5*10^{-2}$ N/m (per unit depth).

Figure 10 presents this force against Reynolds number, with oscillation velocity and extrusion height as length scale. Figure 10a shows the trend of force increase as the amplitude increases. Figure 10b suggests this trend is near linear in the log-log scale.

Further integration of the approach of multiple extrusions on resultant lift is done via increasing spacing between structures – see Fig. 11a. Figure 11b presents results for pressure signature, while Table 2 summarizes the lift calculated for this geometry for all cases considered. Figure 12 further process the data for Fig. 11a in terms of Reynolds numbers, and Figs. 12a & 12b are similar in trend to that of Figs. 10a & 10b.

Comparison of data from Table 1 with Table 2 is noteworthy. The two cases give rise to different vortex formation and, thus, difference in resultant lift values. At low frequency (10Hz.), the lift for the extrusion with larger spacing (Fig. 11a) is greater than that with smaller spacing (Fig. 9a). However, at higher frequencies (100Hz. and 1kHz.) this trend is reversed, although not significantly. Nonetheless, it is well known that vortex interacts strongly with surrounding structure and local flow field. And in this flow scenario, the frequency plays a dominant role in determining the final flow features.

6. Conclusions

Lift generation for MAV via a non-conventional approach is investigated. Instead of some

form of flapping wing or out-of-plane motion, simple in-plane oscillation of a basically flat plate is studied experimentally via a MEMS device and numerically. The key result of this work demonstrated that multiple small extruded structure located on the upper surface of the plate induced vortices that resulted in net lift. The induced vortices might be further be optimized in order to maximize lift generation.

This mechanism for lift in a purely periodic in-plane motion is noteworthy since it should be fairly implementable experimentally, unlike much difficulty encountered for out-of-plane motion. There are various methods to actuate this in-plane motion, e.g. via piezo-based devices. The range of frequency needs to be considered to achieve resonance of the structure. Since results thus far show that the lift increases with frequency, hence, maximization of frequency in consideration of structural resonance should be aimed.

7. Acknowledgement

References
[1] P. Durbin and X. H. Wu, "Transition beneath vortical disturbances," Annu. Rev. Fluid Mech. **39**, 107-128 (2007).
[2] P. R. Spalart, "Airplane trailing vortices," Annu. Rev. Fluid Mech. **30**, 107-138 (1998).
[3] P. B. Rhines, "Vorticity Dynamics of the Oceanic General-Circulation," Annu. Rev. Fluid Mech. **18**, 433-497 (1986).
[4] H. A. Stone, A. D. Stroock, and A. Ajdari, "Engineering flows in small devices: Microfluidics toward a lab-on-a-chip," Annu. Rev. Fluid Mech. **36**, 381-411 (2004).
[5] G. M. Whitesides, "The origins and the future of microfluidics," Nature **442** (7101), 368-373 (2006).
[6] M. Z. Bazant and T. M. Squires, "Induced-charge electrokinetic phenomena: Theory and microfluidic applications," Physical Review Letters **92** (6) (2004).

[7] S. H. Huang, S. K. Wang, H. S. Khoo et al., "AC electroosmotic generated in-plane microvortices for stationary or continuous fluid mixing," Sensors and Actuators B-Chemical **125**, 326-336 (2007).

[8] M. K. Tan, J. R. Friend, and L. Y. Yeo, "Microparticle collection and concentration via a miniature surface acoustic wave device," Lab on a Chip **7** (5), 618-625 (2007).

[9] S. C. Wang, Y. W. Lai, Y. X. Ben et al., "Microfluidic mixing by dc and ac nonlinear electrokinetic vortex flows," Industrial & Engineering Chemistry Research **43** (12), 2902-2911 (2004).

[10] D. T. Chiu, "Cellular manipulations in microvortices," Analytical and Bioanalytical Chemistry **387** (1), 17-20 (2007).

[11] J. P. Shelby and D. T. Chiu, "Controlled rotation of biological micro- and nano-particles in microvortices," Lab on a Chip **4** (3), 168-170 (2004).

[12] J. P. Shelby, S. A. Mutch, and D. T. Chiu, "Direct manipulation and observation of the rotational motion of single optically trapped microparticles and biological cells in microvortices," Analytical Chemistry **76** (9), 2492-2497 (2004).

[13] T. Weisfogh and M. Jensen, "Biology and Physics of Locust Flight. 1. Basic Principles In Insect Flight - A Critical Review." Philosophical Transactions of the Royal Society of London Series B-Biological Sciences 239(667): 415-458 (1956).

[14] W. Shyy, M. Berg, et al., "Flapping and flexible wings for biological and micro air vehicles." Progress in Aerospace Sciences 35(5): 455-505 (1999).

[15] K. V. Rozhdestvensky and V. A. Ryzhov, "Aerohydrodynamics of flapping-wing propulsors." Progress in Aerospace Sciences 39(8): 585-633 (2003).

[16] S. P. Sane, "The aerodynamics of insect flight," Journal of Experimental Biology, 206, 4191-4208 (2003).

[17] S. A. Ansari, R. Zbikowski and K. Knowles, "Aerodynamic Modelling of Insect-like Flapping Flight for Micro Air Vehicles," Progress in Aerospace Sciences, 42, 129-172 (2006).

[18] L. D. Landau and E. M. Lifshitz, *Fluid Mechanics*, 88, (Pergamon Press, 1959).

[19] H. Schlichting, *Boundary-Layer Theory*, 430, (McGraw Hill, 1979).

[20] B.R. Lutz, J. Chen, and D.T. Schwartz, "Hydrodynamic Tweezers: 1. Non-contact cell trapping in a laminar oscillating flow," Anal. Chem. 78 15, 5429-5435 (2006).

[21] Cheng Ming Lin, Yu Shang Lai, Hsin Ping Liu, Chang Yu Chen, and Andrew M. Wo, "Trapping of Bioparticles via Microvortices in a Microfluidic Device for Bioassay Applications," Analytical Chemistry, Vol. 80, pp. 8937-8945 (2008).

[22] Cheng Ming Lin, Yu Shang Lai, Hsin Ping Liu, Andrew M. Wo, "Microvortices and Recirculating Flow Generated by an Oscillatory Microplate for Microfluidic Applications" Applied Physics Letters, Vol. 93, Issue 13, 133503 (2008).

(A)

AC Current

Oscillatory Microplate

Support Beam

Magnetic Field

100 μm

(B)

Sharp Edge

Oscillatory Microplate
(gold-plated)

Si₃N₄

Si

Cavity Magnetic Field B
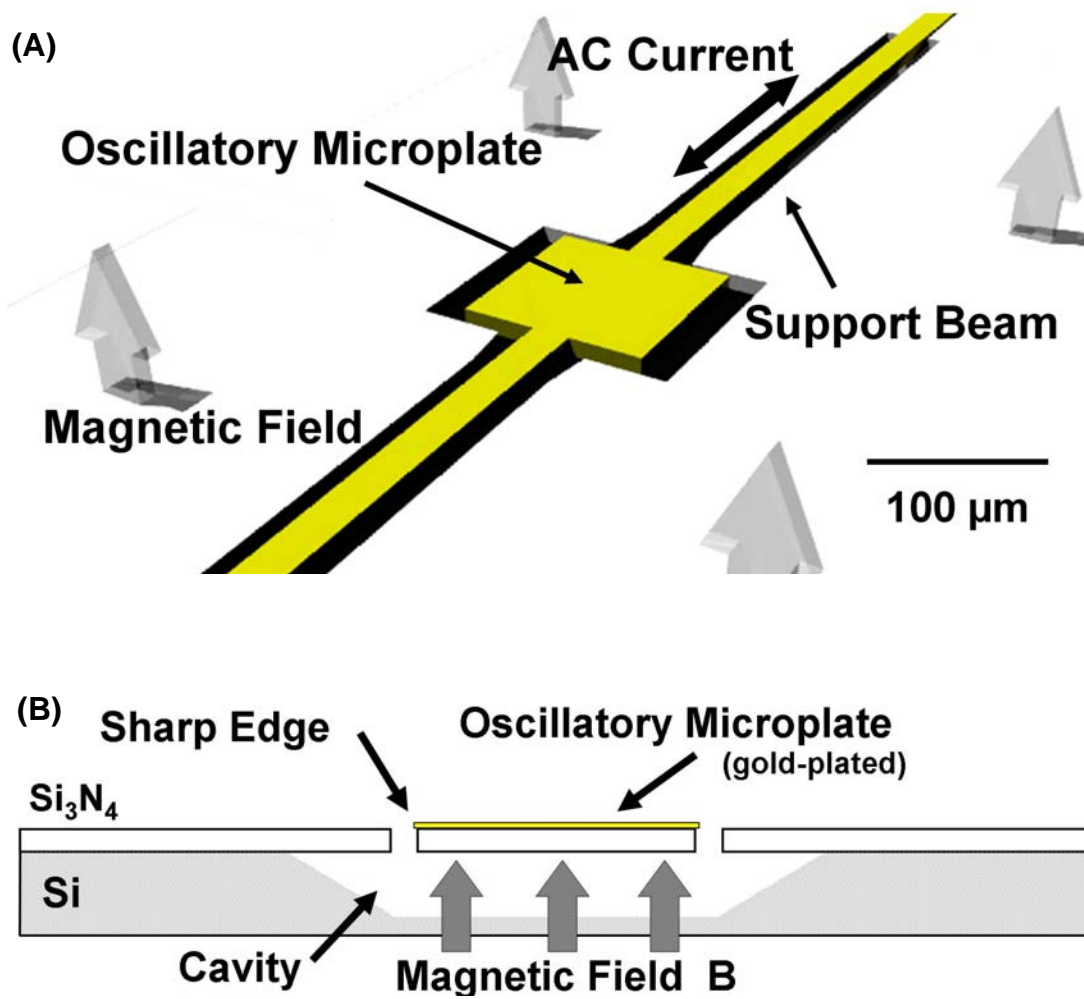
Figure 1. The microdevice. (A) Suspended microplate (100*100*1μm thick) in resonance (140kHz). Plate oscillation is due to Lorentz induced force from AC current flows through the structure above an external magnetic field. (B) Edge-on view showing sharp edges of the microplate, 20μm spacing between microplate and fixed Si₃N₄ structure, cavity underneath, and material details.

a. Deposit silicon nitride

b. Deposit metal layer (Au / Cr)

c. Spin photoresist (PR)

d. Expose and develop PR

e. Etch metal layer

f. Spin (PR)

g. Expose and develop PR

h. Trans pattern with RIE

i. Strip PR

j. KOH wet etching

| Silicon | Si_3N_4 | Metal | Photoresist |
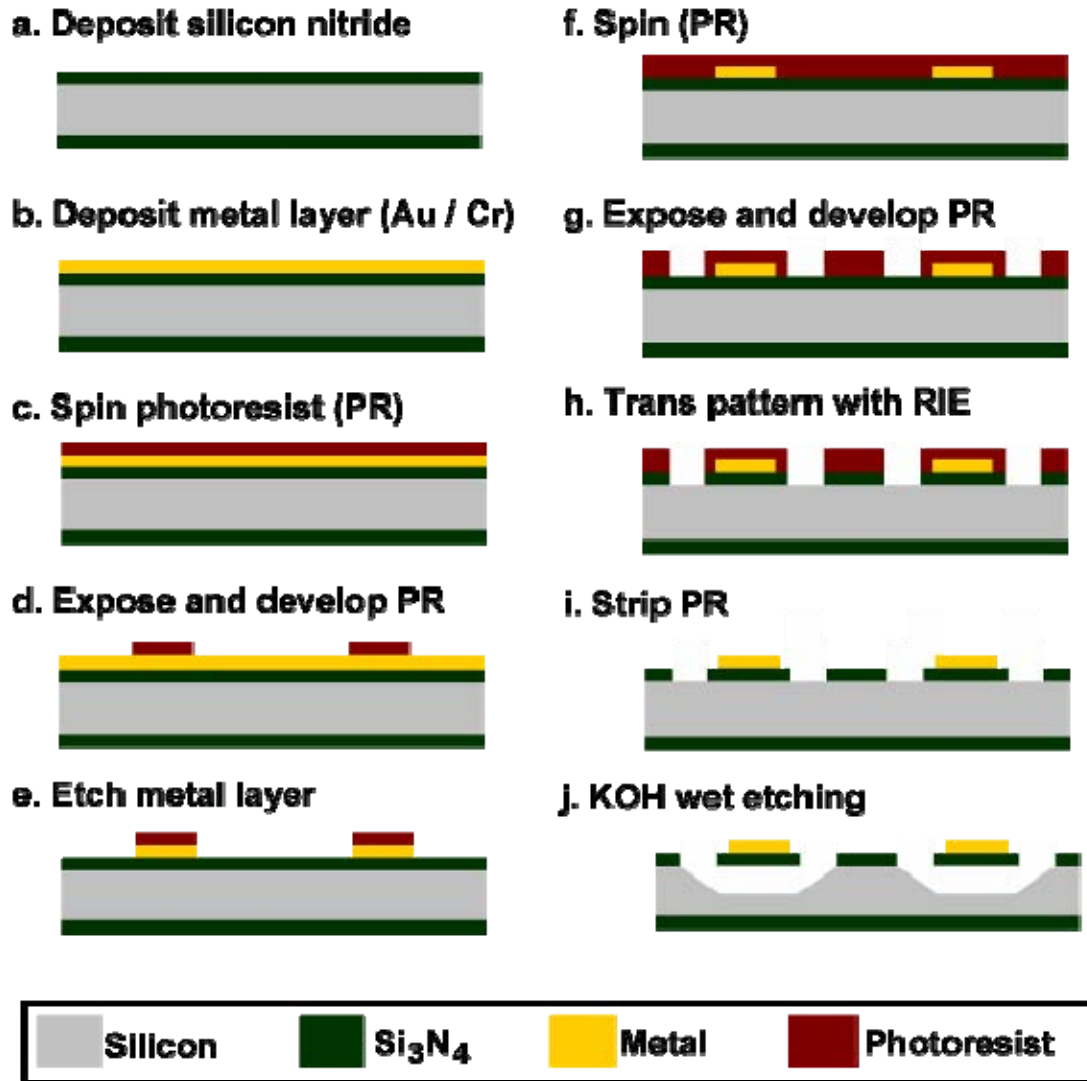
Figure 2. Fabrication processes of the suspended structure. A silicon wafer was used as an experimental substrate. First, the finish on the silicon substrate was silicon nitride (~1µm) (Fig. 2a). Then, a metallic layer (0.15µm thickness of Au/Cr) was sputtered on silicon nitride (Fig. 2b). Moreover, the photoresist (Shipley 1813) layer was patterned for defining the dimension of the electrode (Fig. 2c, d). The element was immerged in the gold and chromium etchant subsequently (Fig. 2e). Next, the positive photoresist on the metal was removed by acetone. By repeating the procedure of coating photoresist (S1813) and development using the MF319 developer (Fig. 2f, g), the cavity underneath the oscillating structure was formed. Therefore, the silicon nitride which was unprotected by the photoresist would be etched using reactive ion etching (RIE) (Fig. 2h). The PR is stripped (Fig. 2i) and etched by utilizing potassium hydroxide (KOH) etchant (Fig. 2j). The suspended structure is finally fabricated.
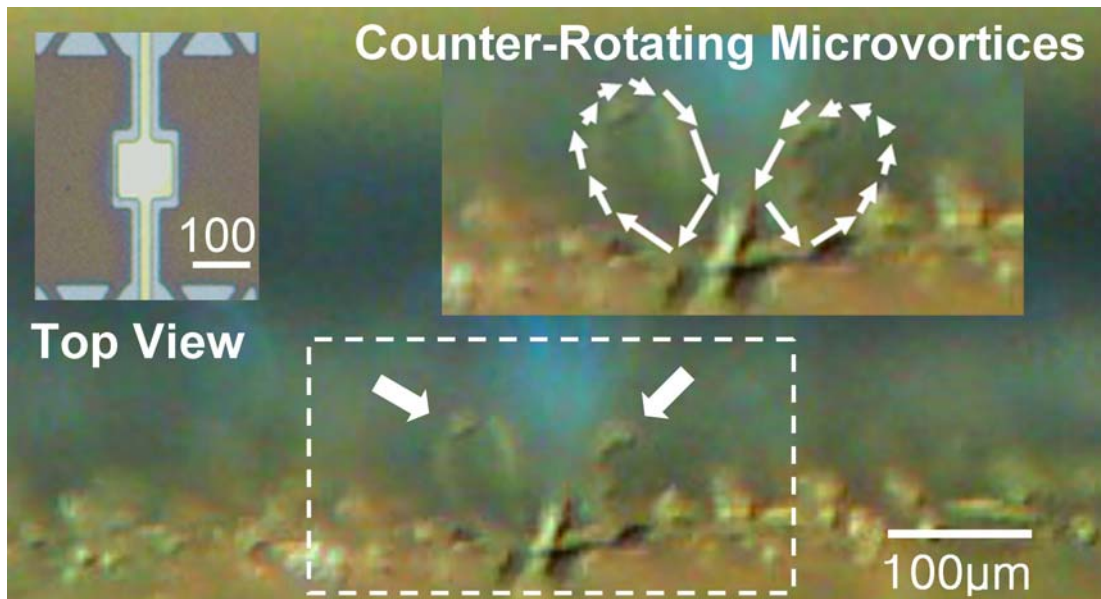
Figure 3. Micrograph revealing counter-rotating microvortices (arrows shown) via tracer particles. The inset (upper left) shows the top view of the device in covered cavity configuration (cover shown in gray regions). Diameter of each vortex (80-100μm) is of order of plate dimension (100μm).
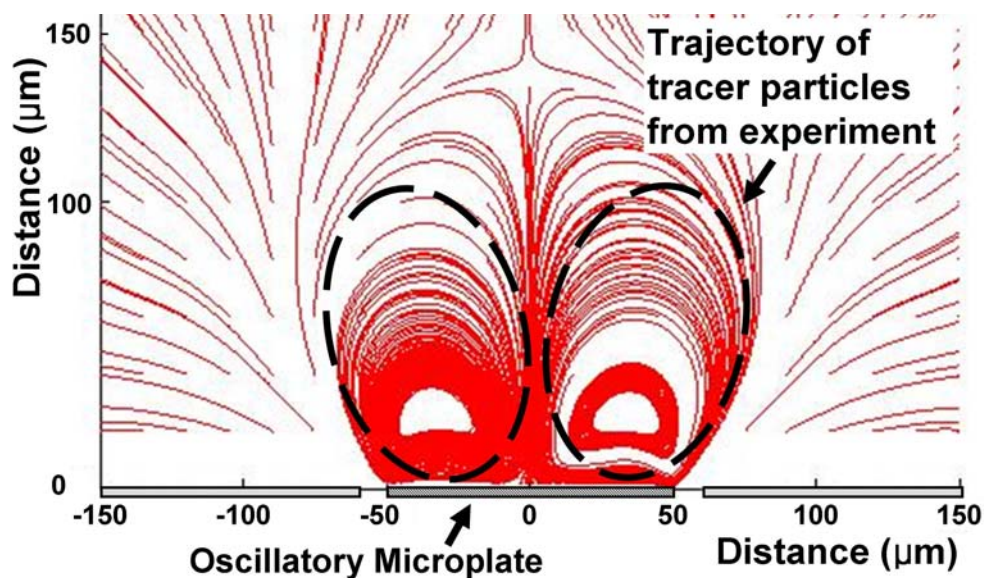
Figure 4. Computational results of the microvortices. Time-mean streamline indicates distinct vortical flow structure. Overlaid are trajectories from tracer particles in the experiment, which show a good match between computed and experimental results of the overall geometry of the microvortices.
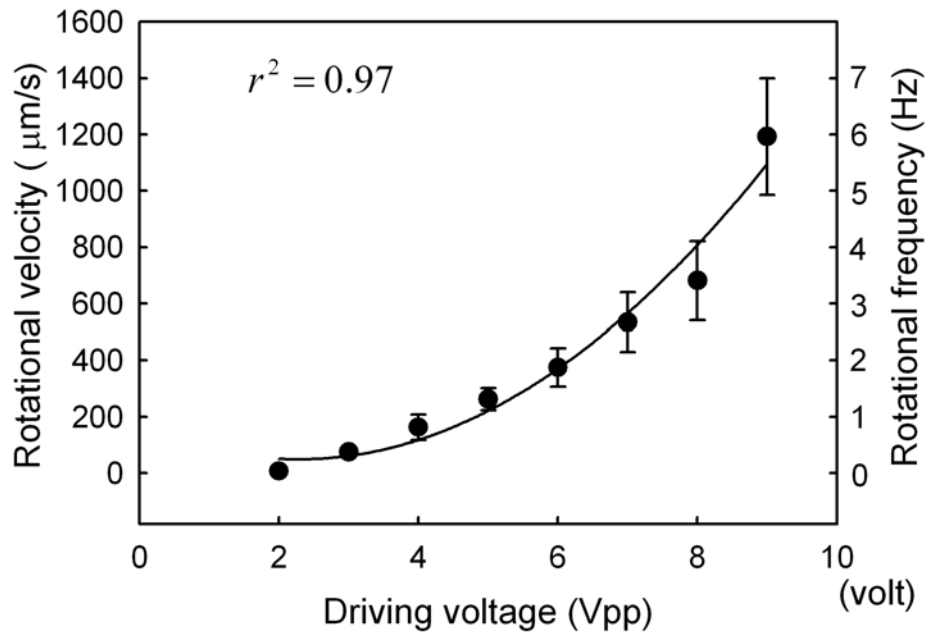
Figure 5. Rotational velocity of a microvortex verses driving voltage (2 to 9Vpp), with corresponding rotational frequency shown on the right ordinate. Results indicated the rotational velocity increases parabolically with voltage. Thus, the microvortex is very controllable, and robust. Statistic analysis performed using Student's t-tests at 95 % confidence level, n = 3, S = 1.0. The regression coefficient is 0.97.

Case 1. Flat plate (control)
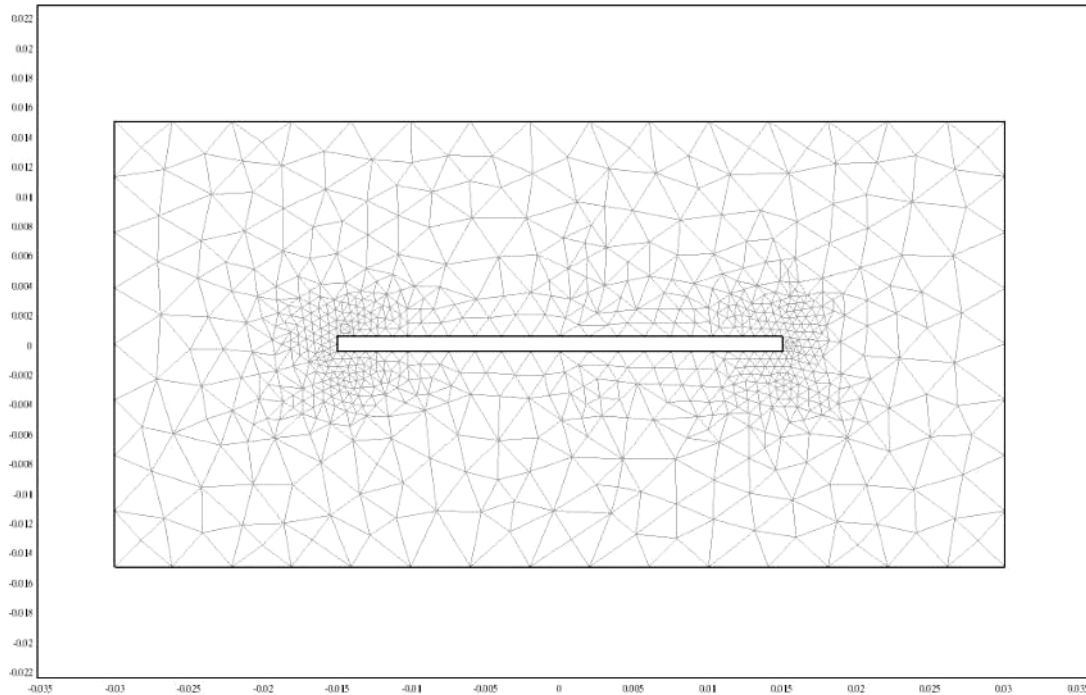
Figure 6a. Mesh of 2D flat plate under in-plane periodic oscillation. Geometric parameters: plate thickness (t)= 1mm (fixed); length of plate= 30mm; frequency= 100Hz; amplitude ratio (δ/t)= 0.1, 0.2, 0.5.
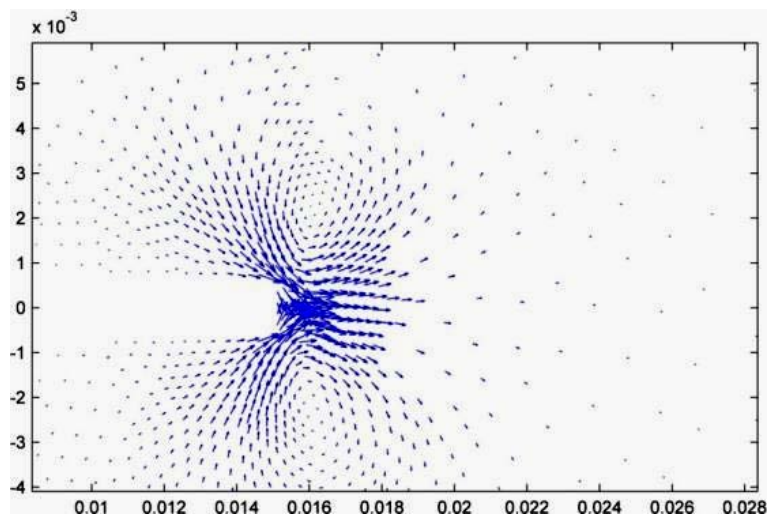
Figure 6b. Time-mean velocity vectors at the plate's right edge showing time-mean microvortices on both the top and bottom regions. This distinct feature corresponds to that observed in the experiment.
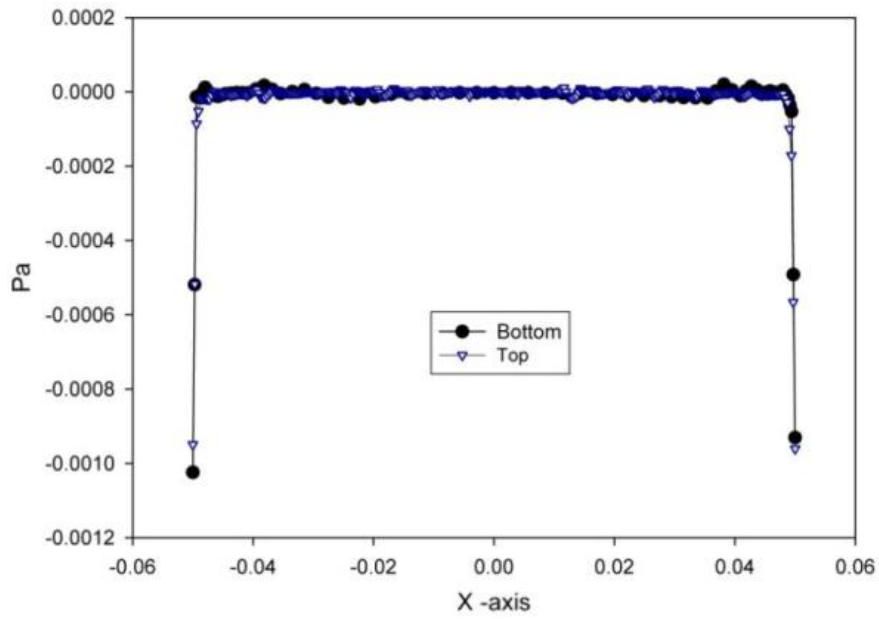
Figure 6c. Time-mean pressure on the top and bottom surfaces. As expected, the pressure trace appears identical; no net pressure difference exists.
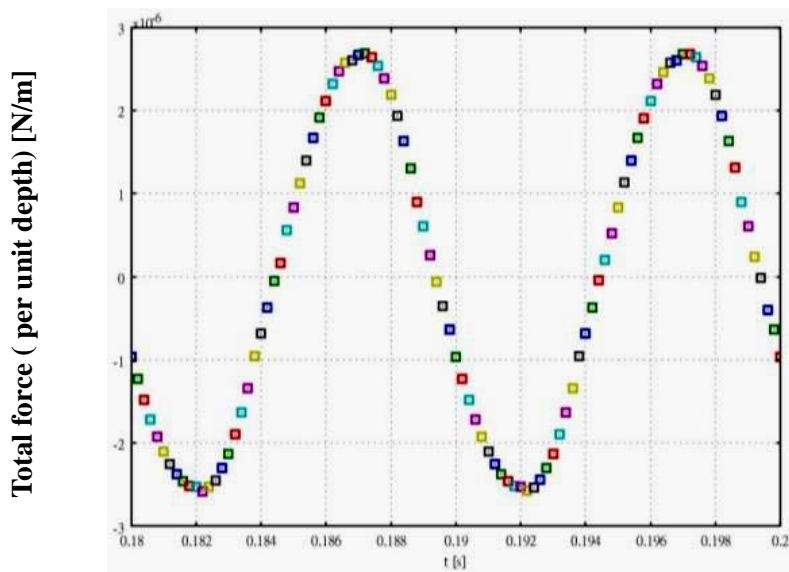
Figure 6d. Time variation of the force on the flat plate, calculated from integration of pressure on both surfaces at each time step. As expected, the pressure trace appears identical; no net pressure difference exists.

Case 2. Tip extrusion structure at the two edges
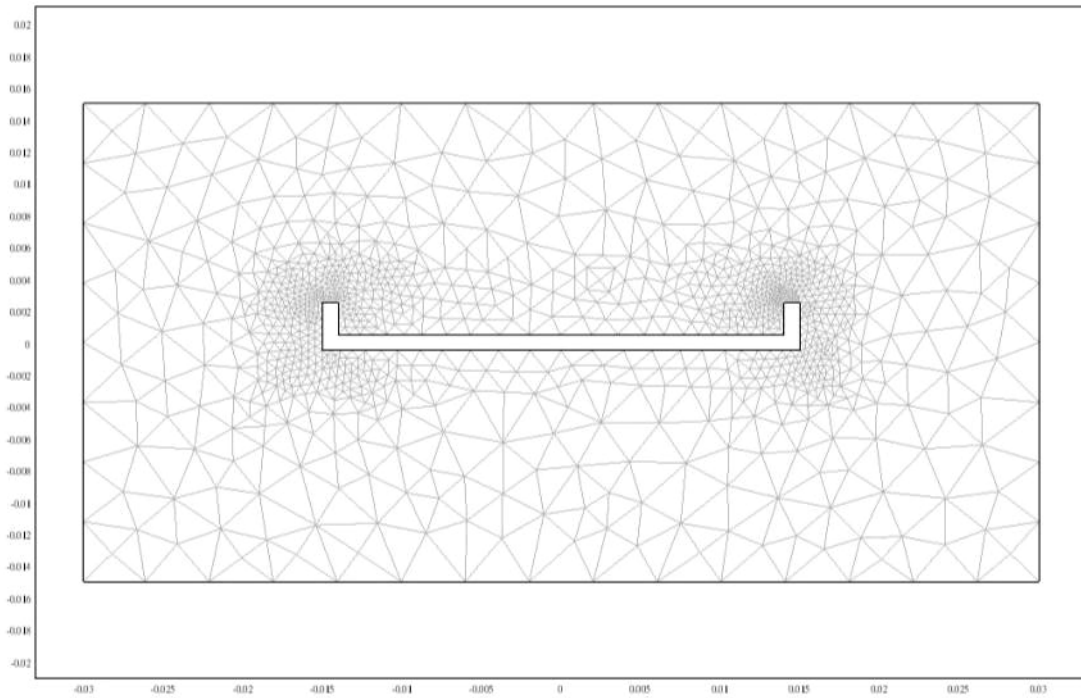
Figure 7a. Extrusion structures are placed on the two edges to encourage spatial gradient, while the entire structure undergoes in-plane periodic oscillation. Geometric parameters: plate thickness (t)= 1mm (fixed); length of plate= 30mm; frequency= 100Hz; amplitude ratio (δ/t)= 0.1.
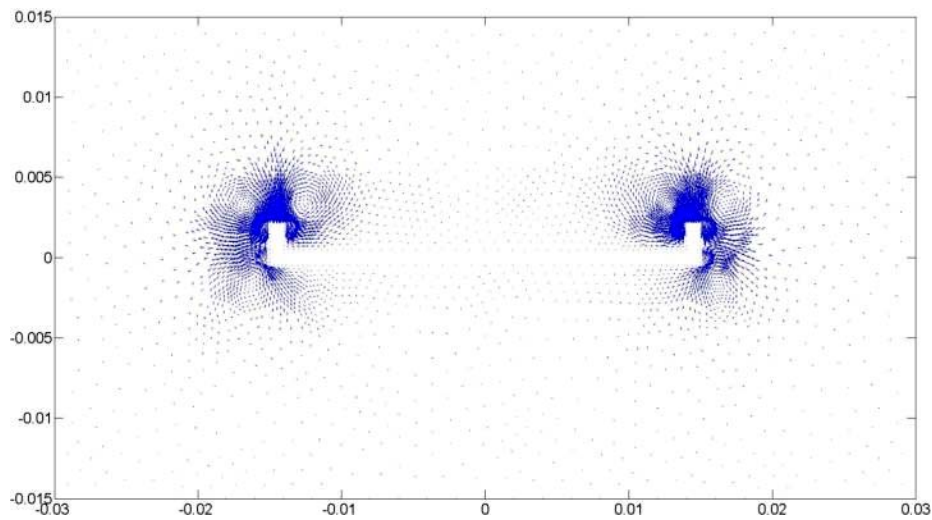
Figure 7b. Time-mean velocity vectors at the plate's edges showing time-mean vortices predominantly on the top surface near the tip structures.
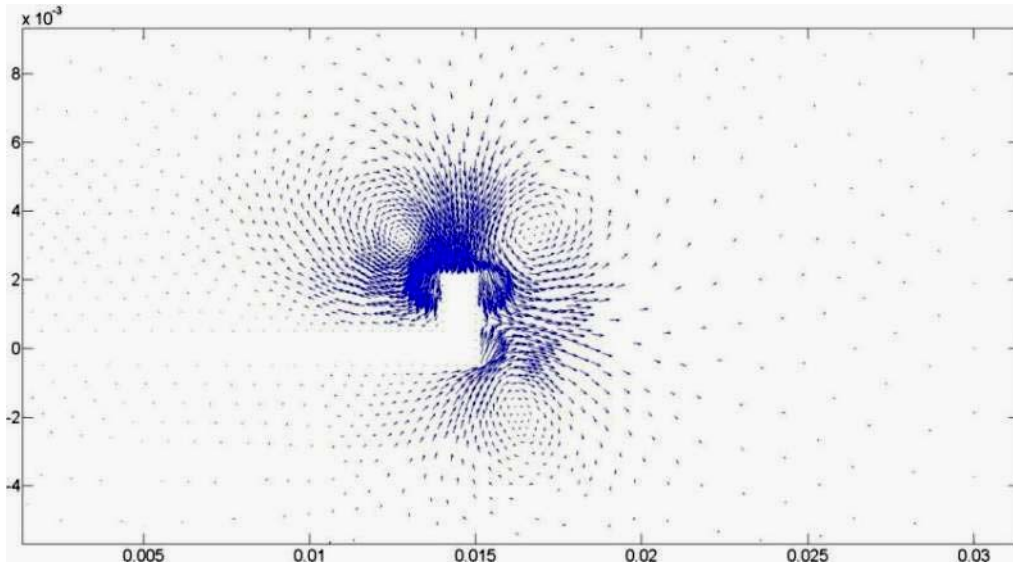
Figure 7c. Close-up of the vortex on the right side of the plate of Fig. 7b.
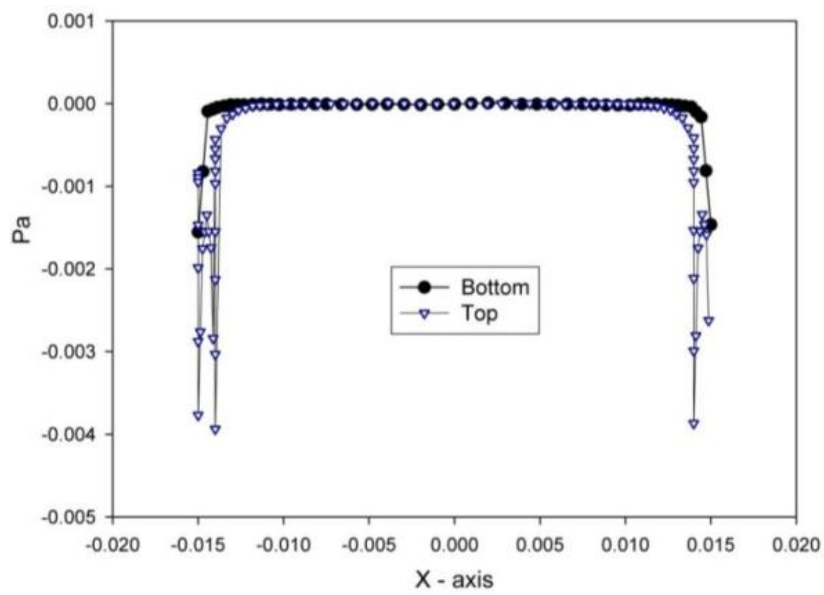
Figure 7d. Time-mean pressure on the top and bottom surfaces. Due to the presence of the tip structure, asymmetry in the pressure signature is shown, unlike that for the purely flat plate case. There exists a relative lower pressure on the extruded structure's edge.
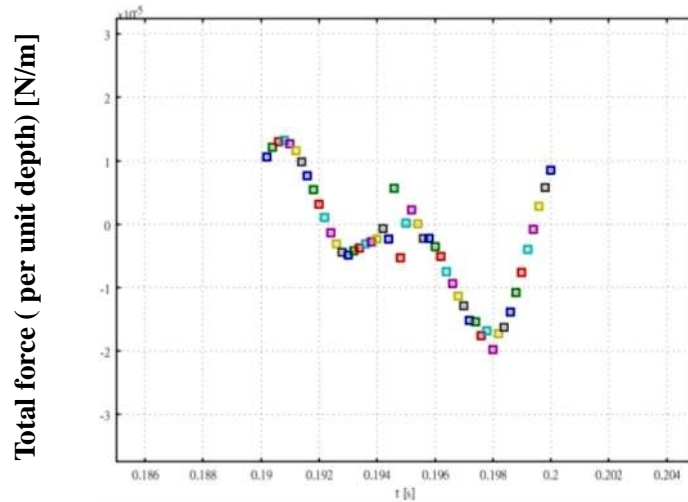
Figure 7e. Time excursion of the integrated force on the entire structure. Due to the presence of the tip structure, asymmetry in the time variation is shown, unlike that for the purely flat plate case. The total force (per unit depth) is **-5.57e-7 N/m** (**f=100hz,** δ **= 0.1t**), which is small. Nonetheless, there seems to have a force resulted from the difference of pressure between the top and bottom surfaces.
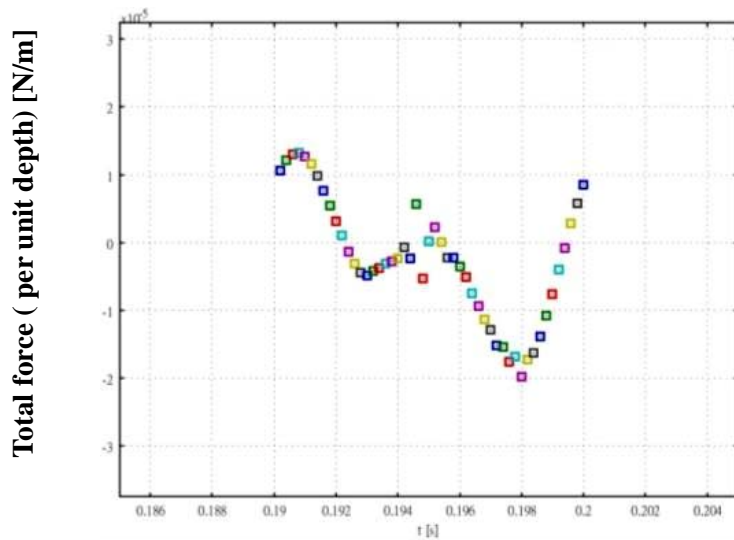
Figure 7f. Time excursion of the integrated force on the entire structure for *increased amplitude* (δ **= 0.2t; f= 100Hz**). Due to the presence of the tip structure, asymmetry in the time variation is shown, unlike that for the purely flat plate case. The total force (per unit depth) is **-2.44e-6 N/m**, larger than that for $\delta = 0.1t$ case.
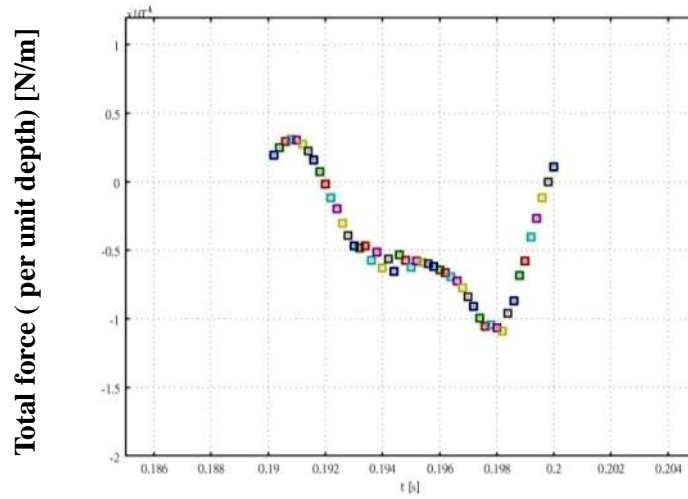
Figure 7g. Time excursion of the integrated force on the entire structure for increased amplitude (δ = **0.5t; f=100Hz**). Due to the presence of the tip structure, asymmetry in the time variation is shown, unlike that for the purely flat plate case. The total force (per unit depth) is **-4.33e-5 N/m**.

Case 3.   A pair of extrusion structure on plate's top surface
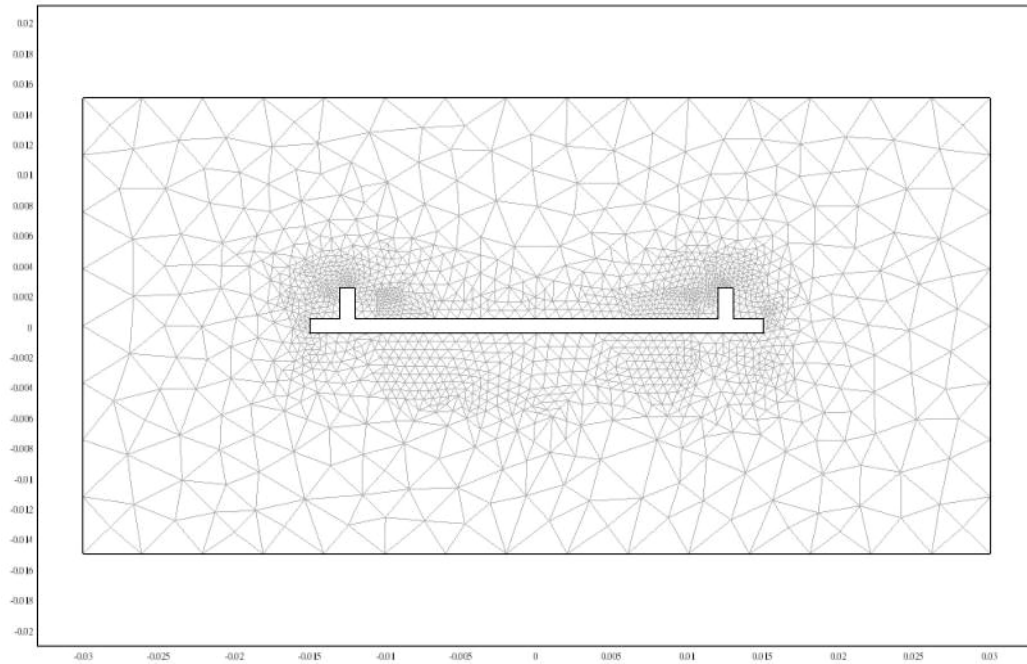
Figure 8a. Mesh of 2D flat plate under in-plane periodic oscillation with a pair of mid-plate extruding structures. Geometric parameters: plate thickness (t)= 1mm (fixed); length of plate= 30mm; frequency= 100Hz.
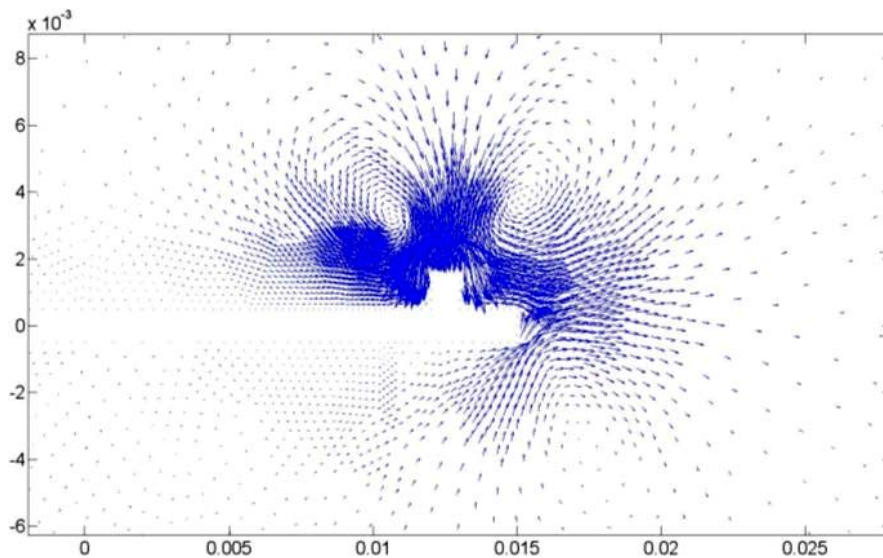
Figure 8b. Time-mean velocity vectors near the plate's extruding structure showing time-mean microvortices on both sides of the extrusion.
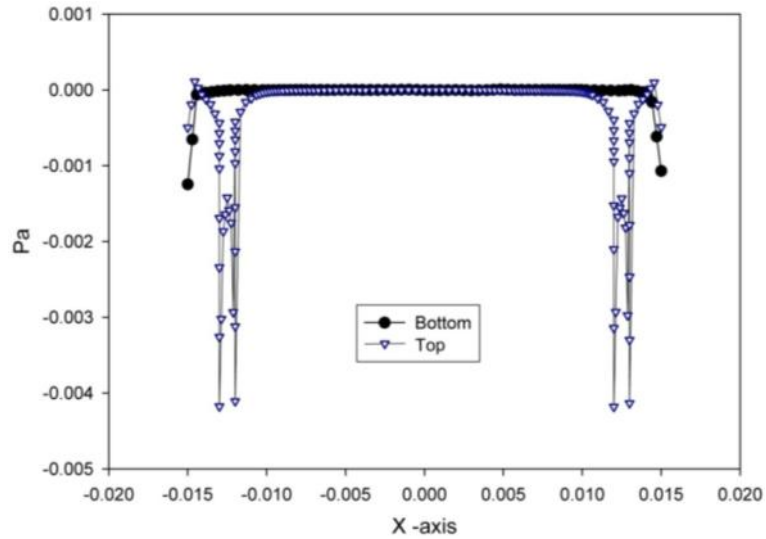
Figure 8c. Time-mean pressure on the top and bottom surfaces. Distinct pressure peaks corresponding to locations of the vortices are clearly seen.
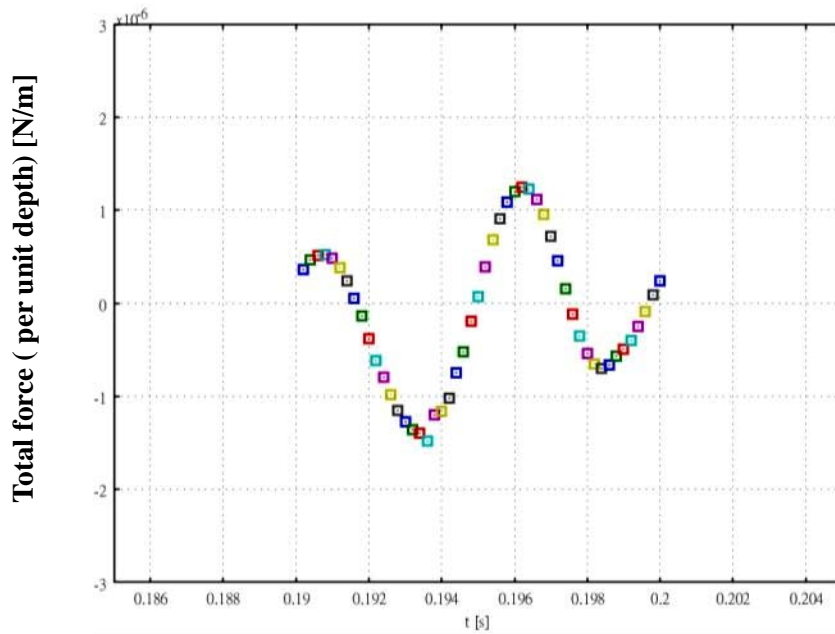
Figure 8d. Time excursion of the integrated force on the entire structure for *increased amplitude* (δ = **0.1t; f= 100Hz**). Due to the presence of extrusion, asymmetry in the time variation is shown, unlike that for the purely flat plate case. The total force (per unit depth) is **-1.17e-7 N/m** – not very significant.

Case 4. Multiple extrusion structure with separation (h)=2*thickness (t)
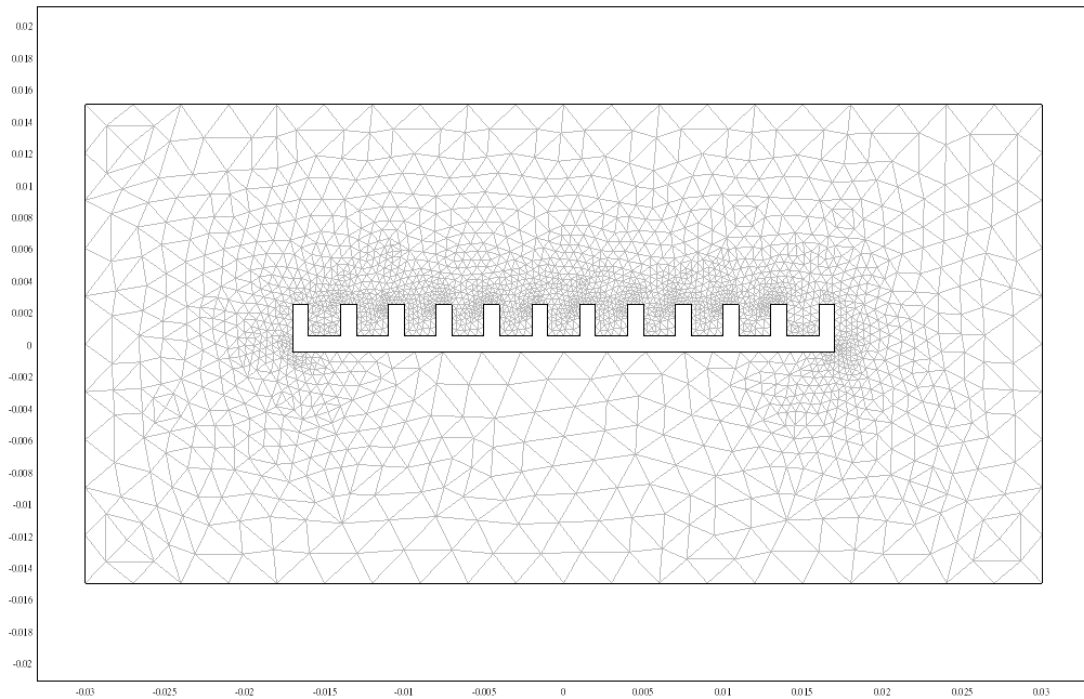
Figure 9a. Mesh of 2D flat plate under in-plane periodic oscillation with multiple mid-plate extruding structures. Geometric parameters: plate thickness (t)= 1mm (fixed); length of plate= 34mm; distance between extruded structure **(h)= 2t**; frequency= 1, 10, 100, 1000Hz; amplitude ratio (δ /t)= 0.1, 0.2, 0.5.
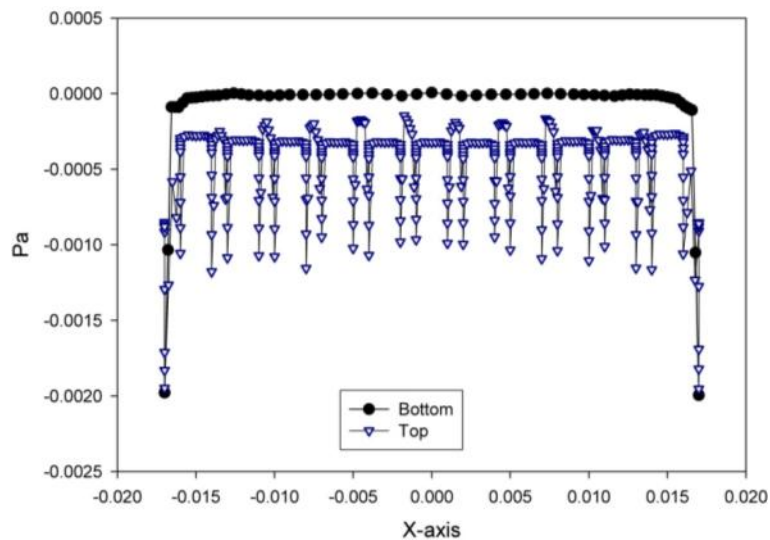
Figure 9b. Typical time-mean pressure distribution on the top and bottom surfaces. Distinct pressure peaks corresponding to locations of a vortex is clearly seen. This pattern of pressure signature is similar over a range of operating conditions, of course, with the exact values of pressure depending on individual cases.
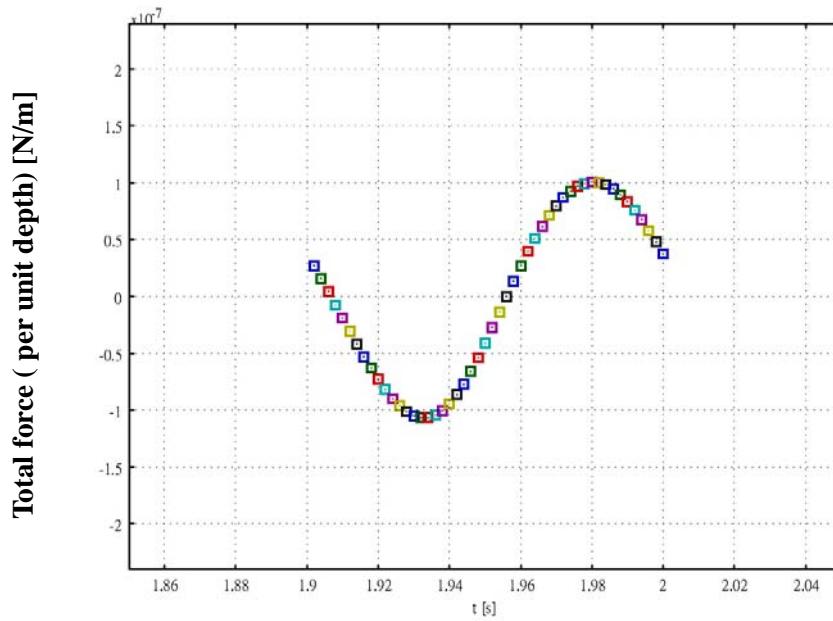
Figure 9c. Time excursion of the integrated force on the entire structure for (δ = **0.1t; f= 10Hz**). Due to the presence of extrusions, asymmetry in the time variation is shown, unlike that for the purely flat plate case. At this low frequency, the total force (per unit depth) is **-5.54e-10 N/m** – not very significant.
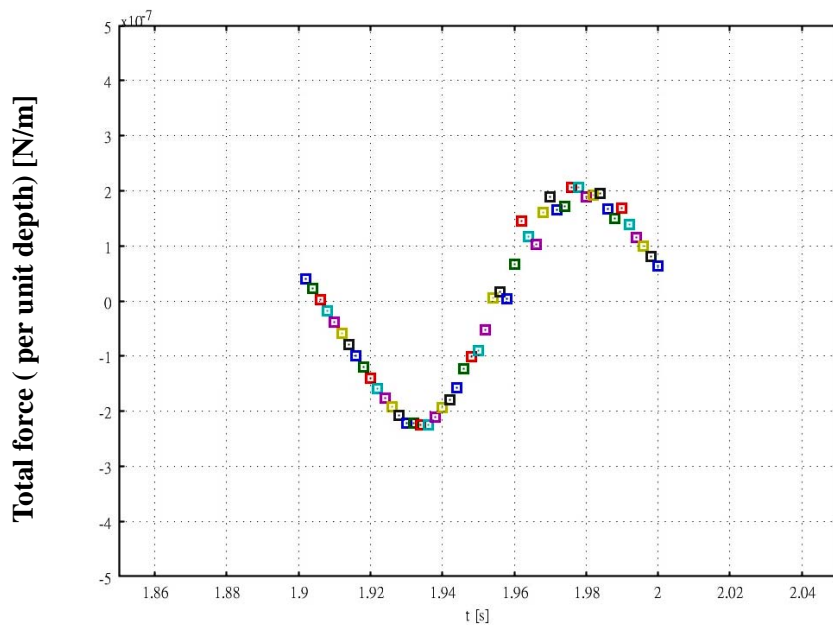

Figure 9d. Time excursion of the integrated force on the entire structure for (δ = **0.2t; f= 10Hz**). Due to the presence of extrusions, asymmetry in the time variation is shown, unlike that for the purely flat plate case. At this low frequency, the total force (per unit depth) is **-1.9e-9 N/m** – not very significant still.

28
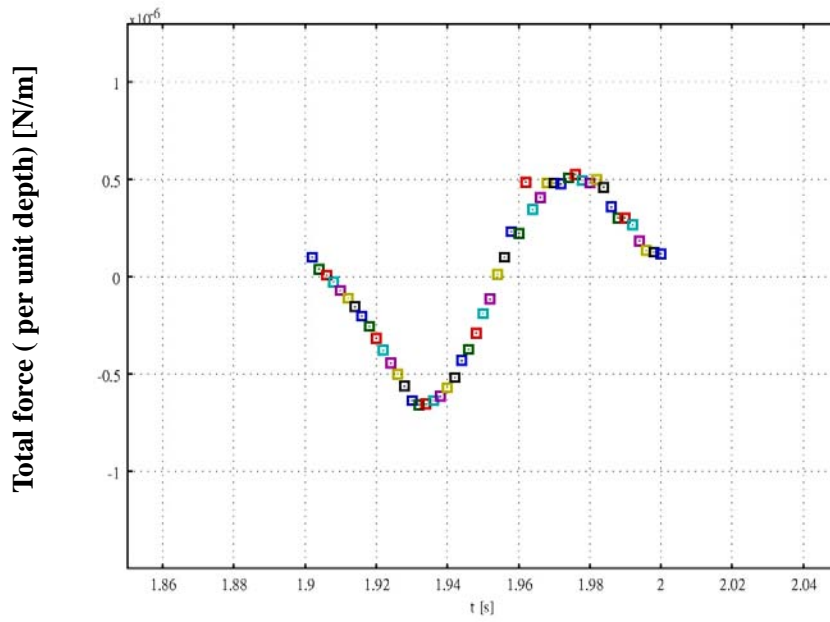
Figure 9e. Time excursion of the integrated force on the entire structure for (δ = **0.5t; f= 10Hz**). Due to the presence of extrusions, asymmetry in the time variation is shown, unlike that for the purely flat plate case. At this low frequency, the total force (per unit depth) is **-1.14e-8 N/m** – not very significant still.
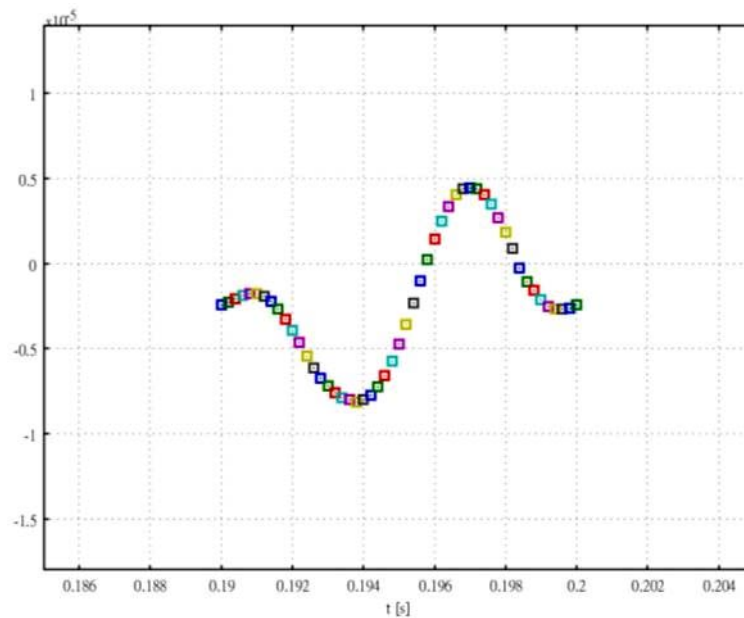

Figure 9f. Time excursion of the integrated force on the entire structure for (δ = **0.1t; f= 100Hz**). Due to the presence of extrusions, asymmetry in the time variation is shown, unlike that for the purely flat plate case. At this low frequency, the total force (per unit depth) is **-2.26e-6 N/m**.
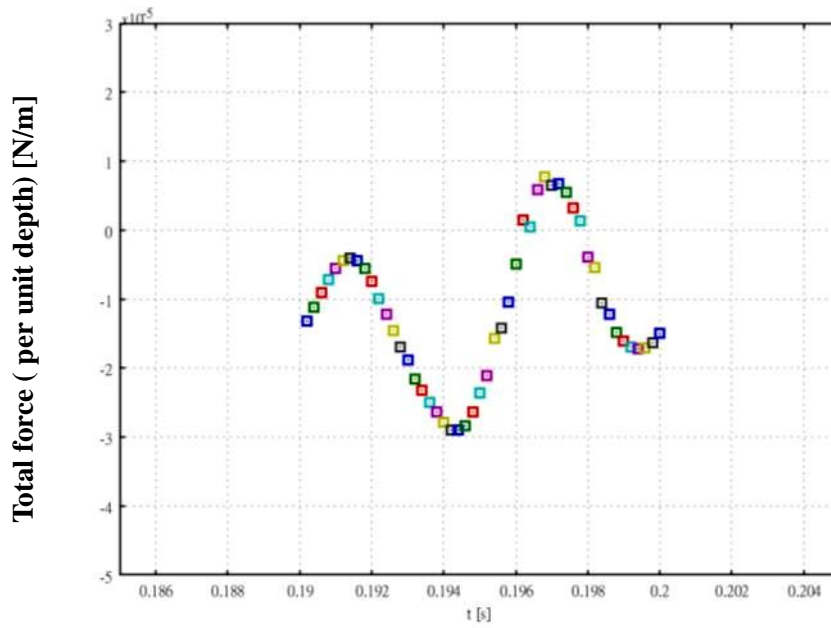
Figure 9g. Time excursion of the integrated force on the entire structure for (δ = **0.2t; f= 100Hz**). Due to the presence of extrusions, asymmetry in the time variation is shown, unlike that for the purely flat plate case. At this low frequency, the total force (per unit depth) is **-1.16e-5 N/m**.
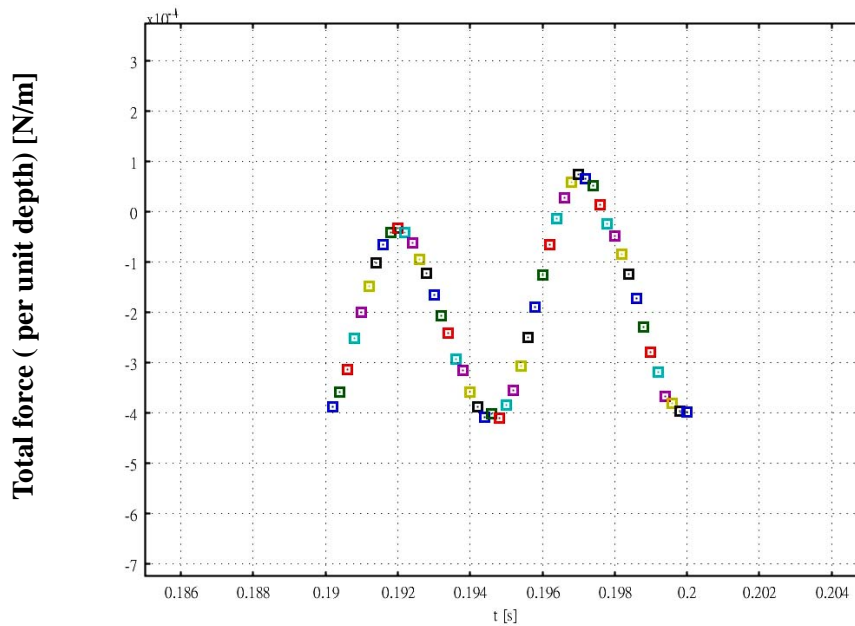

Figure 9h. Time excursion of the integrated force on the entire structure for (δ = **0.5t; f= 100Hz**). Due to the presence of extrusions, asymmetry in the time variation is shown, unlike that for the purely flat plate case. At this low frequency, the total force (per unit depth) is **-1.93e-4 N/m**.
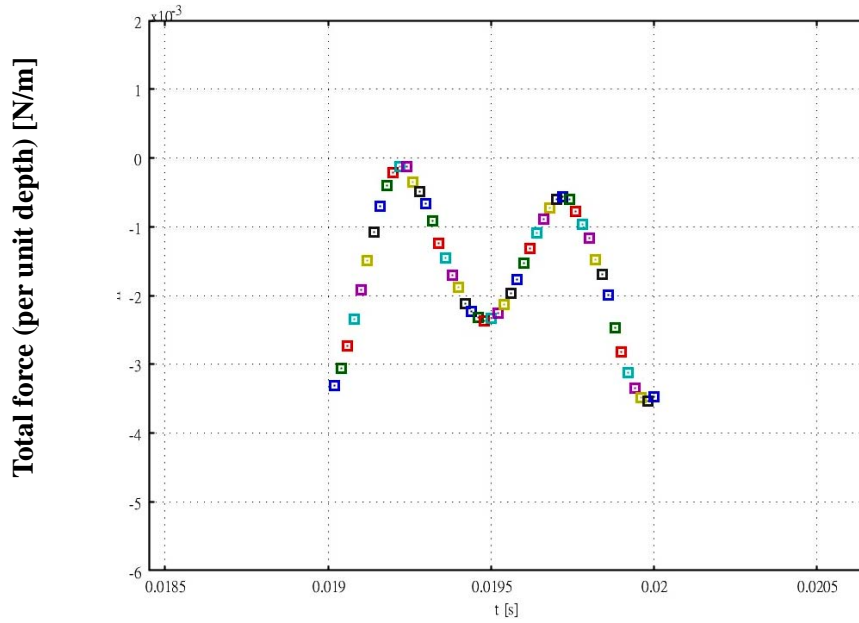
Figure 9i. Time excursion of the integrated force on the entire structure for (δ = **0.1t**; **f= 1000Hz**). Due to the presence of extrusions, asymmetry in the time variation is shown, unlike that for the purely flat plate case. At this low frequency, the total force (per unit depth) is **-1.67*10^{-3} N/m**.
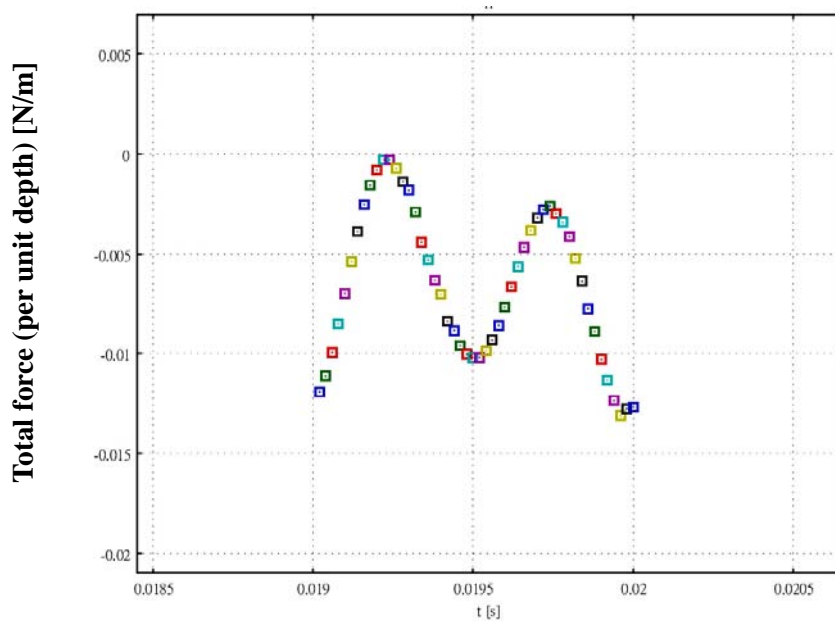
Figure 9j. Time excursion of the integrated force on the entire structure for (δ = **0.2t**; **f= 1000Hz**). Due to the presence of extrusions, asymmetry in the time variation is shown, unlike that for the purely flat plate case. At this low frequency, the total force (per unit depth) is **-6.54*10^{-3} N/m**.
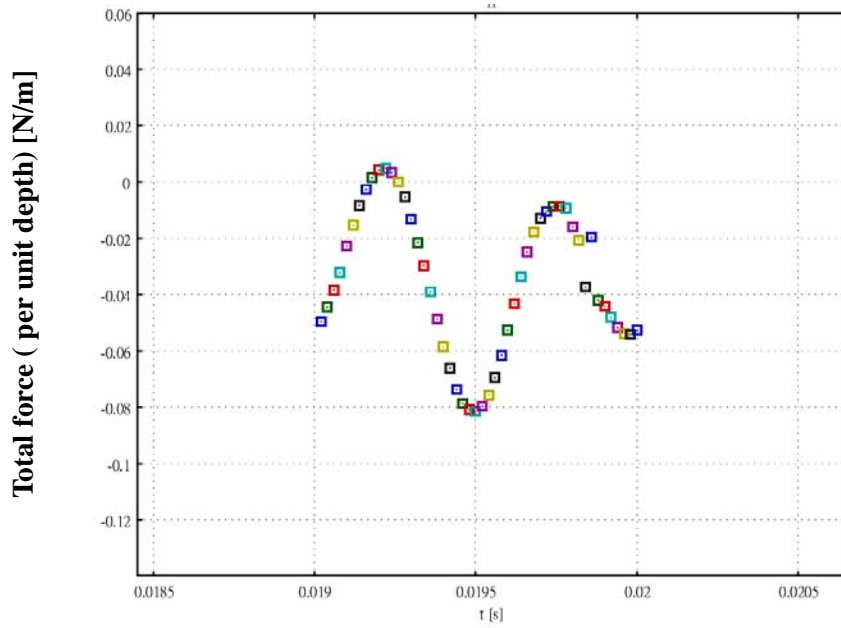
Figure 9k. Time excursion of the integrated force on the entire structure for ($\delta = \mathbf{0.5t}$; $\mathbf{f= 1000Hz}$). Due to the presence of extrusions, asymmetry in the time variation is shown, unlike that for the purely flat plate case. At this low frequency, the total force (per unit depth) is **-3.49*10^{-2} N/m**.

Amplitude	Force acting on the plate (per unit depth; N/m)			
ratio (δ /t)	Freq.= 1 Hz.	10 Hz.	100 Hz.	1000 Hz.
0.1	~ 0	-5.54e-10	-2.26e-6	-1.67e-3
0.2	~ 0	-1.9e-9	-1.16e-5	-6.54e-3
0.5	< 10e-10	-1.14e-8	-1.93e-4	-3.49e-2

Table 1. Force acting on the plate corresponding to that of **Fig. 9a**.
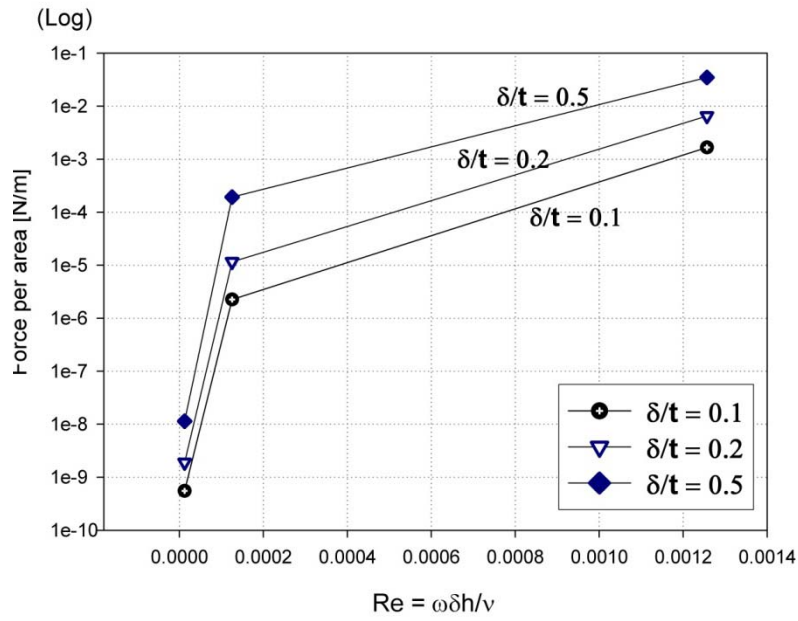
Figure 10a. Dimensionless plot of force (per unit depth) over the range of Reynolds numbers (length scale normalized based on distance between extrusion structures h). Three values of amplitude ratio are shown. Results clearly show strong dependence of dimensionless force with Reynolds number and amplitude ratio.
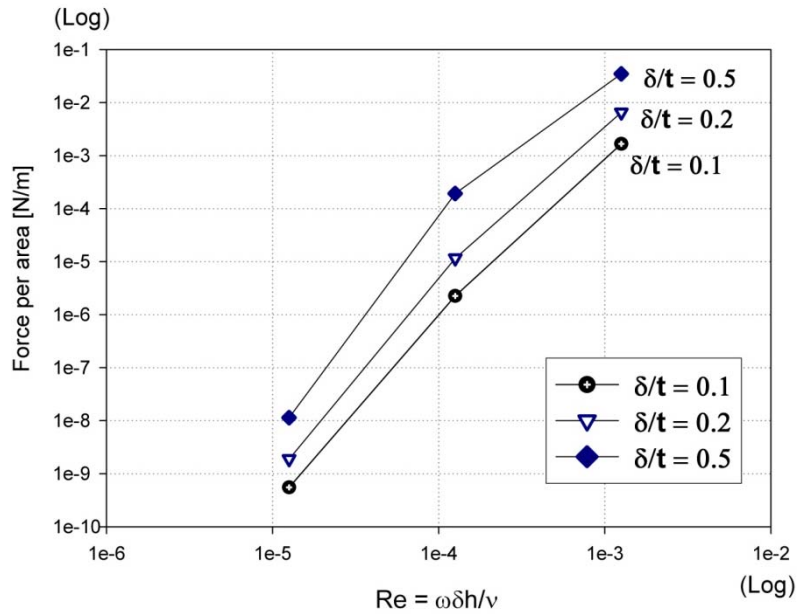

Figure 10b. Same data set as Fig. 10a, except plotted in log-log scale. The near-linearity in this scale is noteworthy.

**Case 5.   Multiple extrusion structure with separation (h)= 4*thickness**
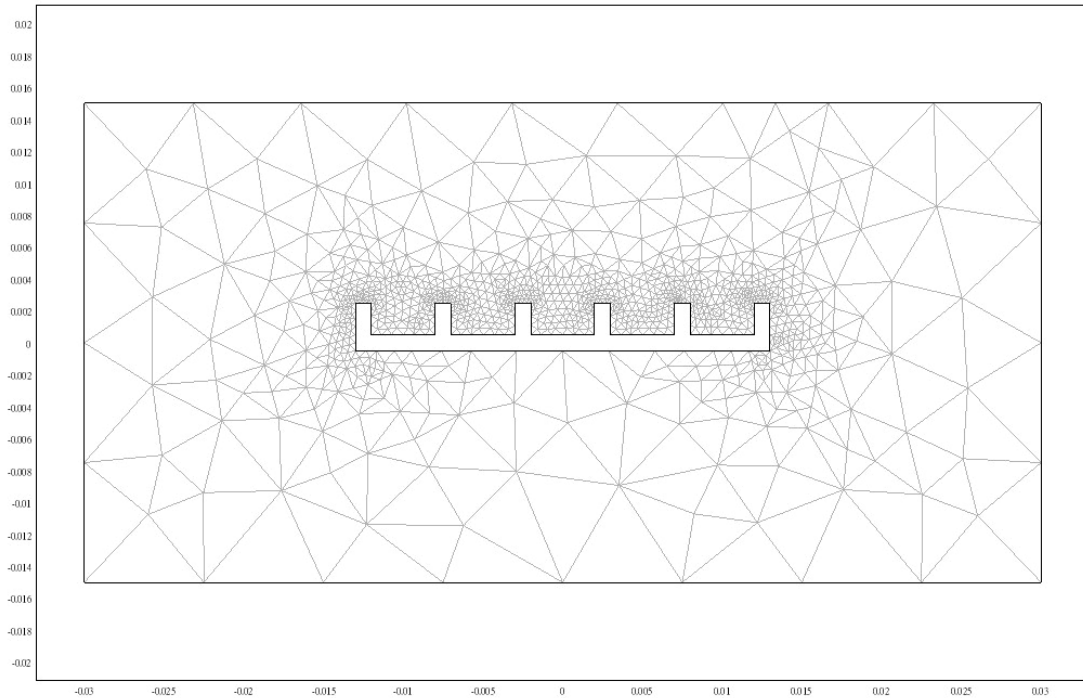
Figure 11a. Mesh of 2D flat plate under in-plane periodic oscillation with multiple mid-plate extruding structures, but each structure further apart than that of Fig. 9a. Geometric parameters: plate thickness (t)= 1mm (fixed); length of plate= 26mm; distance between extruded structure **(h)= 4t**; frequency= 1, 10, 100, 1000Hz; amplitude ratio (δ /t)= 0.1, 0.2, 0.5.
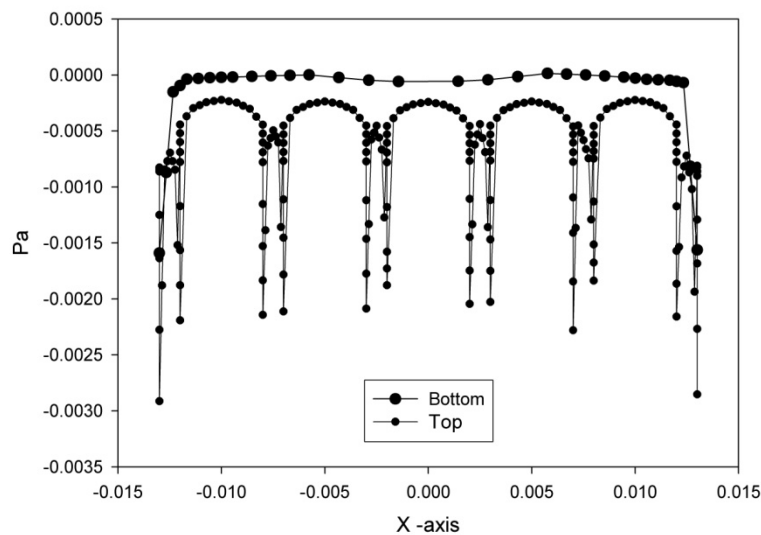

Figure 11b. Typical time-mean pressure distribution on the top and bottom surfaces. Distinct pressure peaks corresponding to locations of a vortex is clearly seen. This pattern of pressure signature is similar over a range of operating conditions, of course, with the exact values of pressure depending on individual cases.

Amplitude ratio (δ/t)	Force acting on the plate (per unit depth; N/m)			
	Freq.= 1 Hz.	10 Hz.	100 Hz.	1000 Hz.
0.1	~ 0	-1.29e-9	-1.37e-6	-1.3e-3
0.2	~ 0	-4.44e-9	-7.44e-6	-4.81e-3
0.5	< 10e-9	-4.63e-8	-9.20e-5	-3.53e-2

Table 2. Force acting on the plate corresponding to that of **Fig. 11a**.
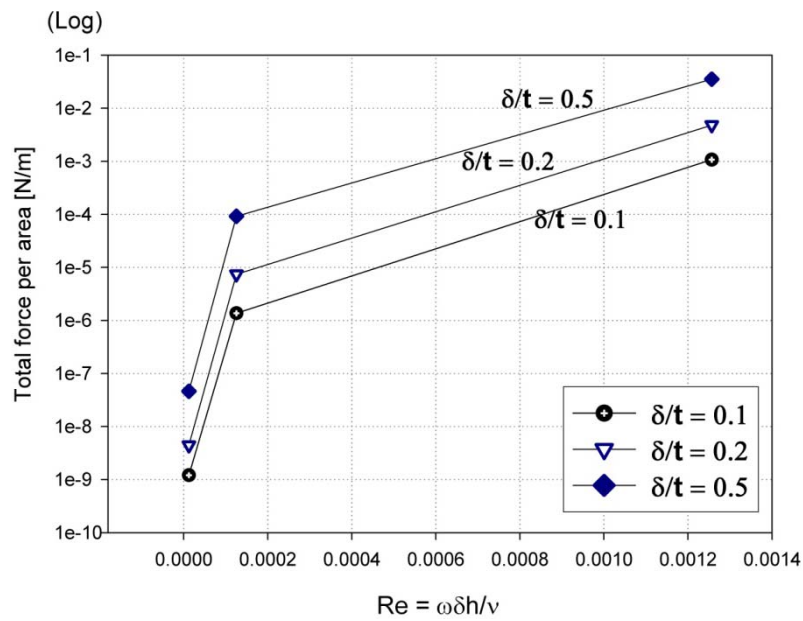

Figure 12a. Dimensionless plot of force (per unit depth) over the range of Reynolds numbers (length scale normalized based on distance between extrusion structures h) corresponding to geometry of Fig. 11a. Three values of amplitude ratio are shown. Results clearly show strong dependence of dimensionless force with Reynolds number and amplitude ratio.
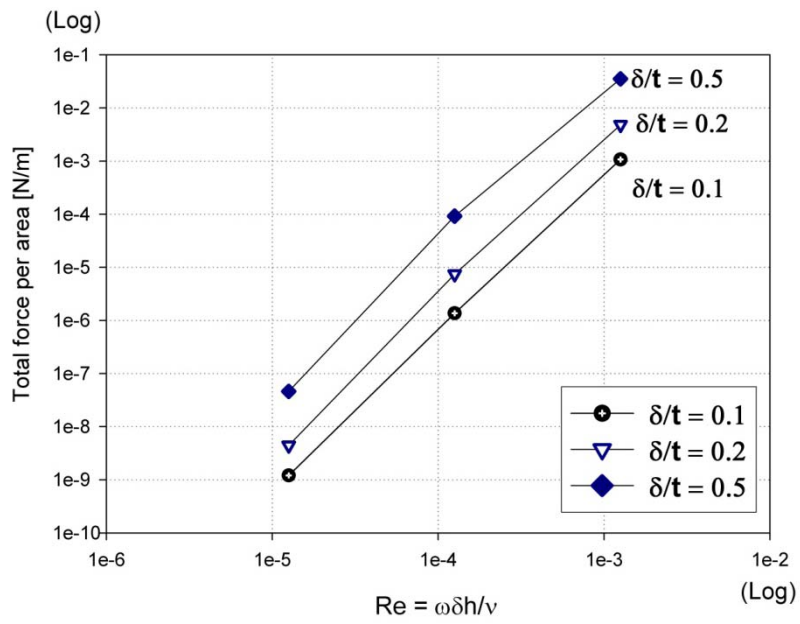
Figure 12b. Same data set as Fig. 12a, except plotted in log-log scale. The near-linearity in this scale is noteworthy.